Sustained phase separation and spin glass in Co-doped $K_xFe_{2-y}Se_2$ single crystals

Hyejin Ryu (류혜진),[1,2,*] Kefeng Wang (王克锋),[1,†] M. Opacic,[3] N. Lazarevic,[3] J. B. Warren,[4]
Z. V. Popovic,[3] Emil S. Bozin,[1] and C. Petrovic[1,2]

[1]*Condensed Matter Physics and Materials Science Department, Brookhaven National Laboratory, Upton, New York 11973, USA*
[2]*Department of Physics and Astronomy, Stony Brook University, Stony Brook, New York 11794-3800, USA*
[3]*Center for Solid State Physics and New Materials, Institute of Physics Belgrade, University of Belgrade,*
Pregrevica 118, 11080 Belgrade, Serbia
[4]*Instrument Division, Brookhaven National Laboratory, Upton, New York 11973, USA*

We present Co substitution effects in $K_xFe_{2-y-z}Co_zSe_2$ ($0.06 \leqslant z \leqslant 1.73$) single-crystal alloys. By 3.5% of Co doping superconductivity is suppressed, whereas phase separation of semiconducting $K_2Fe_4Se_5$ and superconducting/metallic $K_xFe_2Se_2$ is still present. We show that the arrangement and distribution of the superconducting phase (stripe phase) are connected with the arrangement of K, Fe, and Co atoms. Semiconducting spin glass is found in proximity to the superconducting state, persisting for large Co concentrations. At high Co concentrations a ferromagnetic metallic state emerges above the spin glass. This is coincident with changes of the unit cell and arrangement and connectivity of the stripe conducting phase.

I. INTRODUCTION

Since the discovery of high-temperature Fe-based super-conductivity [1], many types of Fe-based superconductors have been reported, including $K_xFe_{2-y}Se_2$ [2,3]. Various novel phenomena were observed by chemical substitution on the Fe site. For example, Co and Ni doping in FeAs tetrahedra of LaFeAsO and $BaFe_2As_2$-based pnictides gives rise to superconductivity [4–7], whereas Co doping in FeSe suppresses superconductivity [8,9]. In particular, $A_xFe_{2-y}Se_2$ (A = K, Cs, Rb, Tl) materials are strongly sensitive to chemical substitutions [10–12].

Among several different types of Fe-based superconductors, $A_xFe_{2-y}Se_2$ (A = K, Cs, Rb, Tl) materials generate significant attention due to unique characteristics such as the absence of the pocket in the Brillouin zone center and phase separation with the Fe-vacancy order where the crystal separates into (super)conducting stripes (block) and magnetic semiconducting matrix regions on the 0.01–100-μm scale [13–18]. The mechanism of the conducting and nonconducting states in proximity to $K_xFe_{2-y}Se_2$ is of great importance for understanding superconductivity [19,20]. Consequently, the details of phase separation, phase stoichiometry, compositions, and their magnetic and electric ground states are currently being debated and are of high interest.

In this study we have investigated $K_xFe_{2-y-z}Co_zSe_2$ ($0.06 \leqslant z \leqslant 1.73$) single-crystal alloys, where y is a Fe/Co vacancy. A rich phase diagram is discovered, where a phase-separated superconducting state of $K_xFe_{2-y}Se_2$ turns into a spin glass and then into a $KCo_{1.73}Se_2$ ferromagnetic metal with no phase separation. We show that the microstructure arrangement and connectivity are rather important for ground-state changes, in addition to changes induced by Co substitution for Fe.

_____
*Present address: Advanced Light Source, E. O. Lawrence Berkeley National Laboratory, Berkeley, California 94720, USA.
†Present address: CNAM, Department of Physics, University of Maryland, College Park, Maryland 20742, USA.

II. EXPERIMENT

Single crystals of $K_xFe_{2-y-z}Co_zSe_2$ ($0.06 \leqslant z \leqslant 1.73$) were synthesized as described previously [21]. Platelike crystals with size up to $10 \times 10 \times 3$ mm^3 were obtained. A high-energy medium-resolution synchrotron x-ray experiment at 300 K was conducted on the X7B beamline of the National Synchrotron Light Source at Brookhaven National Laboratory. The setup utilized an x-ray beam 0.5×0.5 mm in size with a wavelength of 0.3196 Å ($E = 38.7936$ keV) configured with a focusing double-crystal bent Laue monochromator and a Perkin-Elmer amorphous silicon image plate detector mounted perpendicular to the primary beam path. Finely pulverized samples were packed in cylindrical polyimide capillaries 1 mm in diameter and placed 377.81 mm away from the detector. Multiple scans were performed to a total exposure time of 240 s. The two-dimensional (2D) diffraction data were integrated and converted to intensity versus 2θ using the software FIT2D [22]. Structural refinements were carried out using the GSAS modeling program [23] operated by the EXPGUI platform [24]. The backscattered images and energy dispersive x-ray spectroscopy (EDX) mappings were performed in a JEOL-6500 scanning electron microscope (SEM). Electrical transport, thermal transport, heat capacity, and magnetization measurements were carried out in Quantum Design PPMS-9 and MPMS-XL5. Raman scattering measurements were performed on freshly cleaved (001)-oriented samples using TriVista 557 and Jobin Yvon T64000 Raman systems in backscattering micro-Raman configuration. The 514.5-nm laser line of a mixed Ar^+/Kr^+ gas laser was used as an excitation source. All measurements were carried out at room temperature in the vacuum.

III. RESULTS AND DISCUSSION

The obtained high-energy synchrotron x-ray-diffraction data of the $K_xFe_{2-y-z}Co_zSe_2$ series [Fig. 1(a)] can be fitted very well with $I4/m$ and $I4/mmm$ space groups for $z \leqslant 0.92(4)$, while they are fitted by the $I4/mmm$ space group only for $z > 0.92(4)$. This implies coexistence of
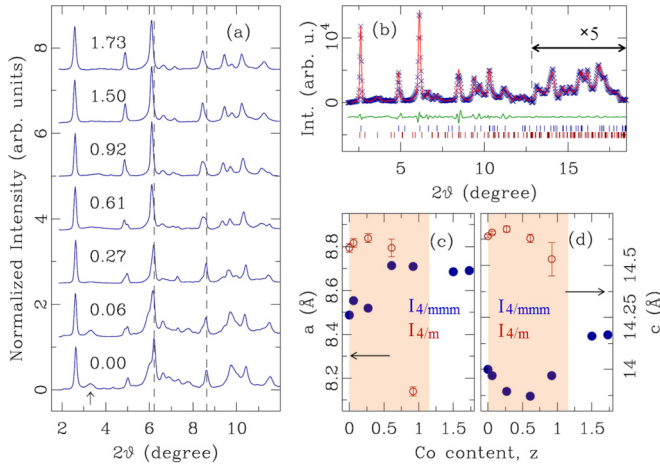
FIG. 1. (Color online) (a) High-energy synchrotron x-ray diffraction data of the $K_x Fe_{2-y-z} Co_z Se_2$ series, normalized by the intensity of (002) reflection for comparison. Data are offset for clarity and labeled by respective Co content as measured by EDX. Vertical dashed lines are provided as a visual reference. Vertical arrow indicates (110) reflection, which is a hallmark of the $I4/m$ phase. Coexistence of the $I4/m$ and $I4/mmm$ phases can be visually tracked up to $z = 0.92(4)$ cobalt content in the samples studied. (b) Modeling of powder diffraction data for a sample with $z = 0.92(4)$. Crosses represent data, red solid line is the model, and green solid line is the difference, which is offset for clarity. Vertical ticks mark the reflections in the $I4/mmm$ (top row) and $I4/m$ (bottom row) phases. (c) and (d) Evolution with EDX-established Co content of refined lattice parameters for $I4/mmm$ (solid blue circles) and $I4/m$ (open red circles). All parameters are expressed in the $I4/m$ metrics (see text). The shaded region is where the signatures of the phase coexistence could be reliably established from the diffraction data.

$I4/m$ and $I4/mmm$ phases when $z \leqslant 0.92(4)$. The typical fit for a phase-separated sample with $z = 0.92(4)$ is shown in Fig. 1(b). Notably, for $0.27 \leqslant z \leqslant 0.92$ intensities of reflections characteristic of the $I4/m$ phase become appreciably weaker and rather broad, indicative of disorder and loss of structural coherence of this structural component, as well as its presumably diminishing contribution. However, quantitative phase analysis was not feasible due to the limited resolution of the measurement and due to the diffuse nature of the signal with broad and overlapping reflections. The evolution of extracted lattice parameters with Co content is shown in Figs. 1(c) and 1(d). Lattice parameters for the a axis of the $I4/mmm$ space group are converted into comparable numbers for the $I4/m$ space group using the formula $I4/m = \sqrt{5}\ I4/mmm$. Nonmonotonic evolution of the lattice parameters highlights the complex crystal structure and bonding in $K_x Fe_{2-y-z} Co_z Se_2$.

The surface morphologies (Fig. 2) show that the Co-doped crystals separate into two regions, a stripe- (domain-) like brighter area that is 1–2 μm thick and a darker matrix area, similar to pure $K_x Fe_{2-y} Se_2$ [17], implying that the phase separation is preserved with Co doping. Distributions of the elements of $K_x Fe_{2-y-z} Co_z Se_2$ in the samples investigated by EDX mapping are shown in Figs. 2(a)–2(c). The bright colored area is the area covered by each element. Se is uniformly distributed for all three samples, while K, Fe, and Co display
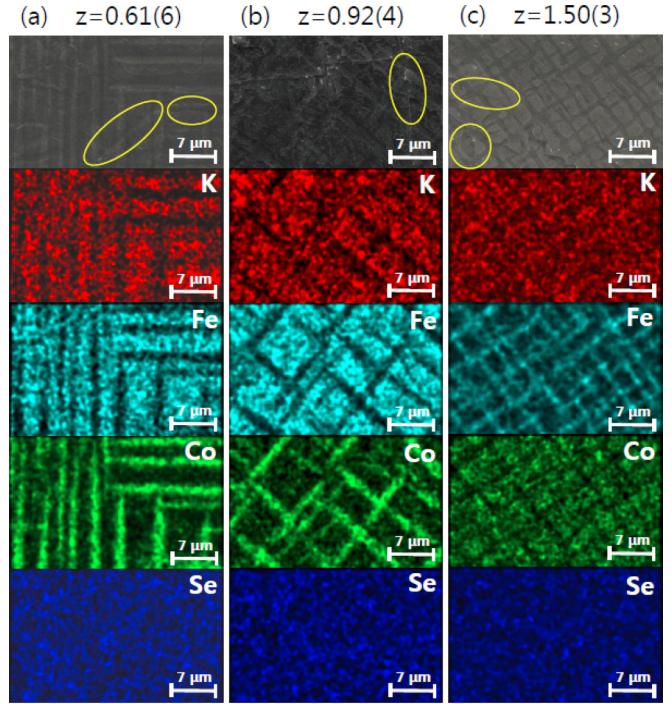

FIG. 2. (Color online) Backscattered electron images of SEM measurement and EDX mappings of $K_x Fe_{2-y-z} Co_z Se_2$ when (a) $z = 0.61(6)$, (b) $z = 0.92(4)$, and (c) $z = 1.50(3)$.

a pattern similar to the backscattered electron image. This suggests that only K, Fe, and Co elements are responsible for phase separation. It is clear that the K and Fe concentrations are lower in the stripes (domains) than in the matrix, while Co concentration is higher in the stripes than in the matrix. Hence, Co atoms prefer to enter into the stripe (domain) phase, which is consistent with the report that Co substitution strongly suppresses superconductivity [12]. The stripe- (domain-) like brighter area maintain its shape across the terraces created by the cleaving, as shown by the marked ellipses in Fig. 2. This may suggest that the stripe- (domain-) like brighter areas form a three-dimensional spider-web-like network [17].

The average stoichiometry was measured by EDX for several single crystals in the same batch with multiple measuring points. The results indicate that the crystals are homogeneous within the scale of around $1 \times 1 \times 0.5$ mm^3. The determined stoichiometries when fixing Se stoichiometry to 2 are shown in Table I. Defects and vacancies of Fe and Co

TABLE I. Summary of measured compositions of $K_x Fe_{2-y-z} Co_z Se_2$ samples.

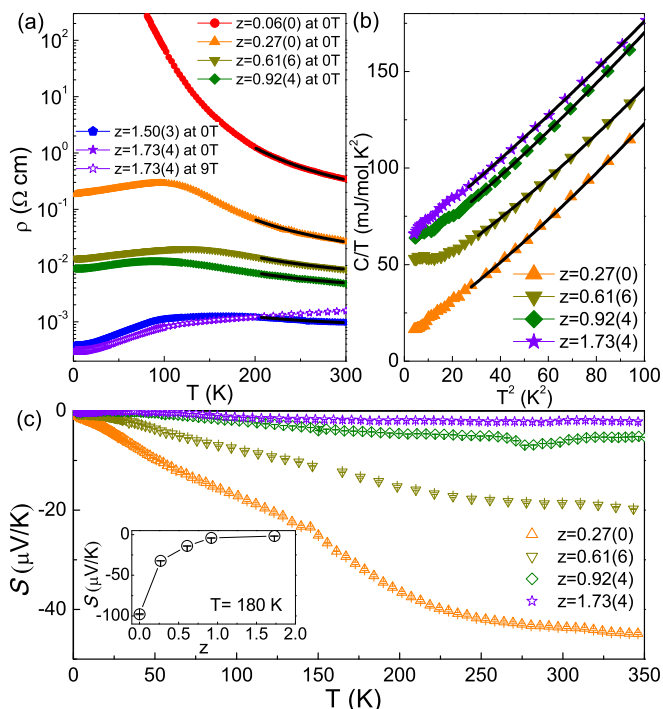| Nominal composition	Measured composition			
K:Fe:Co:Se	K	Fe	Co	Se
1:1.8:0.2:2	0.79(5)	1.37(3)	0.06(0)	2
1:1.4:0.6:2	0.76(1)	1.12(1)	0.27(0)	2
1:1:1:2	0.77(2)	0.92(4)	0.61(6)	2
1:0.6:1.4:2	0.81(2)	0.60(3)	0.92(4)	2
1:0.2:1.8:2	0.78(2)	0.19(1)	1.50(3)	2
1:0:2:2	0.60(6)	0	1.73(4)	2

FIG. 3. (Color online) (a) Temperature dependence of the in-plane resistivity $\rho(T)$ of $K_xFe_{2-y-z}Co_zSe_2$ series at zero (solid symbols) and 9 T field (open symbols). The black solid lines are the fitted result using the thermal activation model. (b) The relation between C/T and T^2 for $K_xFe_{2-y-z}Co_zSe_2$ series at low temperature. The solid lines represent fits by the equation $C/T = \gamma + \beta_3 T^2 + \beta_5 T^4$. (c) Temperature dependence of thermoelectric power $S(T)$ for $K_xFe_{2-y-z}Co_zSe_2$ series. The inset shows the thermoelectric power at $T = 180$ K for different Co concentrations.

are observed for all investigated crystals, which is common in $A_xFe_{2-y}Se_2$ (A = K, Cs, Rb, Tl) compounds [3,25,26]. As the ratio of Co increases, the sum of Fe and the Co ratio slightly increases, while the K ratio remains almost constant, similar to Ni-doped $K_xFe_{2-y}Se_2$ series [27].

As shown in Fig. 3(a), 3.5% of Co doping in $K_xFe_{2-y}Se_2$ completely suppresses the superconductivity and results in a semiconducting $\rho(T)$, consistent with previous research [12]. As Co composition increases, there is a crossover from a semiconductor to metallic state. Besides $K_xCo_{1.73(4)}Se_2$, all other crystals are metallic below a resistivity maximum ρ_{max} and semiconducting above ρ_{max}, similar to $K_xFe_{2-y}Se_{2-z}S_z$ [21]. The high-temperature part (above 200 K) of $\rho(T)$ can be fitted by the thermal activation model $\rho = \rho_0 \exp(E_a/k_BT)$, where ρ_0 is a prefactor, E_a is an activation energy, and k_B is Boltzmann's constant [Fig. 3(a)]. The obtained ρ_0 and E_a are listed in Table II and are mostly smaller than values for $K_xFe_{2-y}S_2$ and $KFe_{0.85}Ag_{1.15}Te_2$ [25,28].

The heat capacity of the $K_xFe_{2-y-z}Co_zSe_2$ series also exhibits the crossover from semiconductor to metal as Co increases, consistent with resistivity [Fig. 3(b)]. $C/T-T^2$ relations between 5 and 10 K can be fitted by the formula $C/T = \gamma + \beta_3 T^2 + \beta_5 T^4$. The Debye temperatures are obtained from $\Theta_D = (12\pi^4 NR/5\beta)^{1/3}$, where N is the atomic number in the chemical formula and R is the gas constant. The obtained γ values and Debye temperatures Θ_D for different

TABLE II. Summary of ρ_0 values and activation energy E_a in $K_xFe_{2-y-z}Co_zSe_2$.

z	ρ_0 (mΩ cm)	E_a (meV)
0.06(0)	24.3(4)	67.7(4)
0.27(0)	4.20(9)	47.1(5)
0.61(6)	3.07(1)	26.6(1)
0.92(4)	2.15(3)	21.4(3)
1.50(3)	0.597(7)	12.4(2)

Co ratios are listed in Table III. The Debye temperature for the $K_xFe_{2-y-z}Co_zSe_2$ series are similar, suggesting that there are no considerable changes in atomic weight, structure, and bonding. A small γ value for $z = 0.27(0)$ implies a low density of states at the Fermi level, similar to typical semiconductors, while large γ values for $z \geqslant 0.92(4)$ suggest accumulation of the density of states, as expected in metals.

Thermoelectric power $S(T)$ of the $K_xFe_{2-y-z}Co_zSe_2$ series shows negative values for all different Co concentrations, which reveals that dominant carriers are electrons [Fig. 3(c)]. The magnitude of $S(z)$ decreases as the Co ratio increases to around 50% [$z = 0.92(4)$] and saturates [inset in Fig. 3(c)]. There are no obvious peaks in the thermoelectric power for the $K_xFe_{2-y-z}Co_zSe_2$ series between 2 and 350 K, suggesting that there are no dramatic Fermi surface changes.

The temperature-dependent dc magnetic susceptibilities of the $K_xFe_{2-y-z}Co_zSe_2$ series show irreversible behaviors between zero-field cooling (ZFC) and field cooling (FC) at low temperature [Fig. 4(a)]. This is a typical behavior of a spin glass in magnetic field caused by the frozen magnetic spins in random directions below the characteristic temperature T_f. Insets in Figs. 4(a) and 4(b) also suggest a spin glass due to the linear field dependence of the magnetic susceptibility with no hysteresis above T_f (measured at 300 K) and an S-shaped loop of the $M-H$ curve below T_f (measured at 1.8 K). Hence, 3.5% Co doping ($z = 0.06$) not only suppresses superconductivity but also may result in a spin glass. Ferromagnetic behavior appears when $z \geqslant 1.50(3)$ [29]. High-temperature regions ($T \geqslant 150$ K) of the $K_xFe_{2-y-z}Co_zSe_2$ series follow the Curie-Weiss law $\chi(T) = \chi_0 + C/(T-\theta)$, where χ_0 includes core diamagnetism and van Vleck and Pauli paramagnetism, C is the Curie constant, and θ is the Curie-Weiss temperature [Figs. 4(a) and 4(b)]. The obtained parameters are summarized in Table IV. Negative θ values are observed even for crystals that order ferromagnetically, suggesting prevalent antiferromagnetic interactions probably come from the localized moment of the block (stripe) domain due to the phase separation.

TABLE III. Summary of γ values and Debye temperatures of $K_xFe_{2-y-z}Co_zSe_2$.

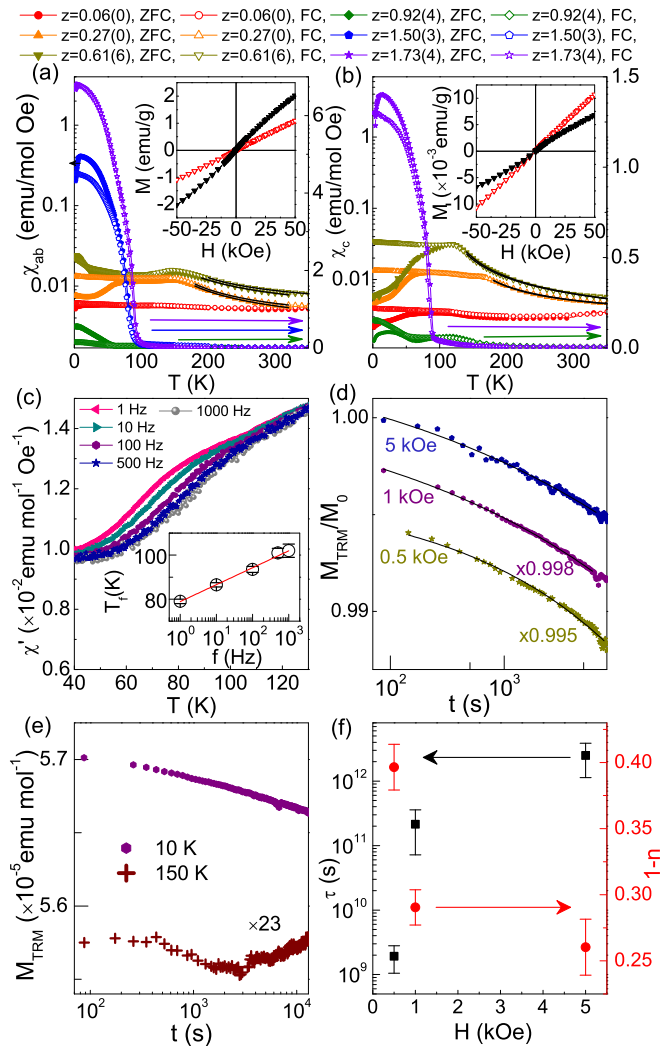| z	γ (mJ mol^{-1} K^{-2})	Θ_D (K)
0.27(0)	11(1)	220(4)
0.61(6)	38(1)	227(3)
0.92(4)	54(1)	215(3)
1.73(4)	63(1)	213(2)

FIG. 4. (Color online) Temperature dependence of dc magnetic susceptibilities of $K_x Fe_{2-y-z} Co_z Se_2$ series for (a) $H \perp c$ and (b) $H \| c$ at $H = 1$ kOe in ZFC and FC below 350 K. Insets in (a) and (b) are $M-H$ curves of $K_x Fe_{2-y-z} Co_z Se_2$ with $z = 0.61(6)$ for $H \perp c$ and $H \| c$, respectively, at 1.8 K (black solid inverse triangle) and 300 K (red open inverse triangle). (c) Temperature dependence of ac susceptibility $\chi'(T)$ measured at five different frequencies for $z = 0.27(0)$ of $K_x Fe_{2-y-z} Co_z Se_2$. The inset shows the frequency dependence of T_f with the linear fitting (solid line). (d) TRM vs time for $z = 0.27(0)$ of $K_x Fe_{2-y-z} Co_z Se_2$ at 10 K and $t_w = 100$ s with different dc fields with fittings using stretched exponential function (solid lines). (e) M_{TRM} vs t at 10 and 150 K with $H = 1$ kOe and $t_w = 100$ s. (f) H-field dependence $\tau(s)$ (black solid square) and $1 - n$ (red solid circle).

Confirmation of the spin glass comes from the frequency dependence of the real part of ac susceptibility and thermoremanent magnetization. The frequency-dependent susceptibility $\chi'(T)$ is shown in Fig. 4(c). As frequency increases, the characteristic temperature T_f peak position increases, whereas its magnitude decreases [30]. The frequency dependence of the peak shift is fitted by $K = \Delta T_f / (T_f \Delta \log f)$ (Fig. 4), and the obtained K value is 0.036(1), in agreement with the canonical spin-glass values ($0.0045 \leqslant K \leqslant 0.08$) [30]. Thermoremanent magnetization (TRM) is shown in Fig. 4(d).

TABLE IV. Summary of χ_0, effective moment μ_{eff}, and θ values from Curie-Weiss fitting of $K_x Fe_{2-y-z} Co_z Se_2$.

z		χ_0 (emu mol^{-1}Oe^{-1})	μ_{eff} (μ_B/Fe)	θ (K)
0.27(0)	$H \perp c$	$2.4(2) \times 10^{-3}$	2.33(8)	−91(5)
	$H \| c$	$2.7(1) \times 10^{-3}$	1.88(6)	−118(3)
0.61(0)	$H \perp c$	$1.6(1) \times 10^{-3}$	2.76(3)	−98(1)
	$H \| c$	$3.7(4) \times 10^{-3}$	2.79(9)	−81(9)
0.92(4)	$H \perp c$	$3.6(4) \times 10^{-3}$	2.7(2)	−120(9)
	$H \| c$	$2.8(1) \times 10^{-3}$	2.38(2)	−146(1)
1.50(3)	$H \perp c$	$9.9(1) \times 10^{-3}$	1.42(4)	−218(2)
	$H \| c$	$8.2(2) \times 10^{-3}$	0.65(9)	−257(6)
1.73(4)	$H \perp c$	$7.9(9) \times 10^{-4}$	3.2(4)	−86(9)
	$H \| c$	$2.9(8) \times 10^{-3}$	1.8(6)	−138(9)

The sample was cooled down from 200 K (above T_f) to 10 K (below T_f) in four different magnetic fields, then kept at 10 K for $t_w = 100$ s. After that, the magnetic field was removed, and $M_{TRM}(t)$ was measured. As observed in Fig. 4(d), $M_{TRM}(t)$ decays very slowly for all three different magnetic fields towards its nonzero equilibrium value [30]. On the other hand, $M_{TRM}(t)$ measured at 150 K (above T_f) relaxes quickly in a short time [less than $\sim$100 s; Fig. 4(e)]. Slow relaxation behavior is fitted well by the stretched exponential function, $M_{TRM}(t) \sim M_0 \exp[-(t/\tau)^{1-n}]$, where M_0, τ, and $1 - n$ are the glassy component, the relaxation characteristic time, and the critical exponent, respectively. As shown in Fig. 4(f), the obtained τ increases as the H field increases, while $1 - n$ stays close to 1/3, consistent with theoretical and experimental results for a spin-glass system [31,32].

Figure 5(a) shows polarized Raman scattering spectra of a $K_{0.6} Co_{1.73} Se_2$ single crystal measured from the (001) plane for the two sample orientations at 100 K using the Jobin Yvon T64000 Raman system. According to selection rules for the $I4/mmm$ space group, peaks at about 174 and 184 cm^{-1} (at 100 K) are assigned as B_{1g} and A_{1g} Raman modes, respectively [33,34].

Unpolarized Raman scattering spectra of $K_x Fe_{2-y-z} Co_z Se_2$ single crystals are presented in Fig. 5(b). For $z = 1.73(4)$ samples, only two peaks, which were assigned as A_{1g} ($\sim$180 cm^{-1}) and B_{1g} ($\sim$169 cm^{-1}) modes, can be observed in the Raman spectrum. These modes are also observed for $z = 1.50(3)$ and $z = 0.92(4)$ samples. In fact, the A_{1g} mode can be observed in Raman spectra for all concentrations of cobalt, suggesting that superconducting/metallic $K_x Fe_2 Se_2$ phase is present in all investigated samples. The energy of this mode does not change significantly by varying concentrations of Co or for different transition-metal ions [33,34]. For the intermediate concentration [$0.61(6) \leqslant z \leqslant 1.50(3)$] a broad structure around 250 cm^{-1} has been observed, which probably originates from the crystalline disorder in the semiconducting $K_2 Fe_4 Se_5$ phase. In general, high disorder may cause relaxation of the selection rules, resulting in the appearance of broad asymmetric structures. With further decreasing the Co concentration [$z \leqslant 0.27(0)$], a large number of Raman modes can be clearly observed in the spectra in addition to the A_{1g} mode of the superconducting/metallic $K_x Fe_2 Se_2$ phase. These
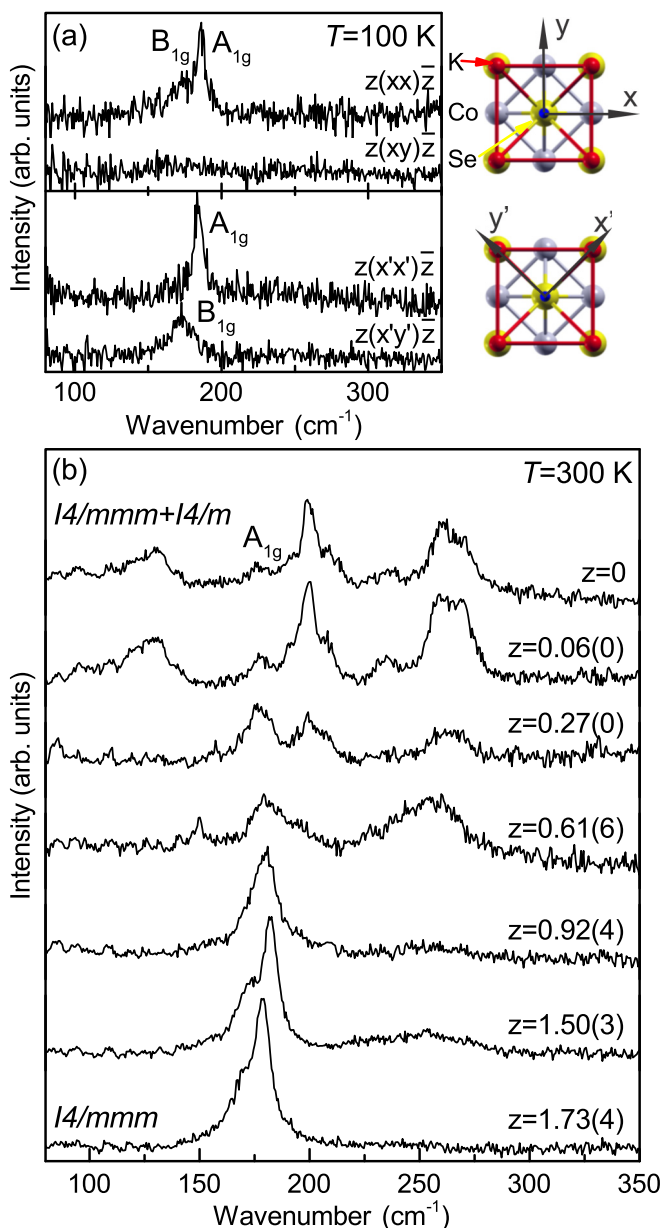
FIG. 5. (Color online) (a) Raman scattering spectra of $K_{0.6}Co_{1.73}Se_2$ single crystals in various scattering configurations ($\mathbf{x} = [100], \mathbf{y} = [010], \mathbf{x'} = 1/\sqrt{2}[110], \mathbf{y'} = 1/\sqrt{2}[1\bar{1}0]$). (b) Raman scattering spectra of $K_xFe_{2-y-z}Co_zSe_2$, $[0 \leqslant z \leqslant 1.73(4)]$ single crystals measured at room temperature from the (001) plane of the samples.

FIG. 6. (Color online) Magnetic and transport phase diagram. Open squares and open circles are spin-glass characteristic temperature T_f for the $H \perp c$ and $H \parallel c$ directions, respectively. Open triangles are the ferromagnetic transition temperature, and open diamonds are the thermoelectric power S_T at 180 K. Open hexagons are resistivity maximums ρ_{max}, which show the semiconductor (brighter yellow region) to metal (darker orange region) crossover. The lines at the top denote the regions of the ordered $I4/m$ and $I4/mmm$ space groups.

modes originate from the lattice vibrations within the ordered low-symmetry semiconducting $K_2Fe_4Se_5$ phase [33,35].

The magnetic and transport phase diagram of $K_xFe_{2-y-z}Co_zSe_2$ series is presented in Fig. 6. When $z \sim 0$ there is superconductivity below $T_c \sim 30$ K and metallic resistivity below and semiconducting above about 125 K [3]. By 3.5% Co doping, not only is superconductivity completely suppressed, but so is conductivity with emerging spin-glass magnetic order below $T_f \sim 70$ K in 1 kOe. A semiconducting/bad-metal spin glass is found in proximity to the superconducting state, similar to copper oxides. As Co
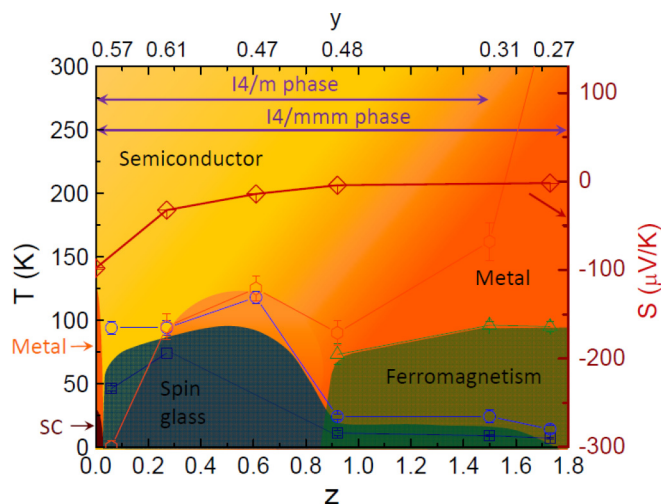
concentration increases, the spin-glass state is maintained, while the semiconductor to metal crossover is present at low temperatures up to $z \sim 0.6$. After that, the spin glass and metallicity decrease up to $z \sim 0.9$. With a further increase in Co concentration, metallic conductivity spreads to higher temperatures, while the spin glass is suppressed to the lower-temperature region (below ~ 20 K), and the ferromagnetic ground state emerges above the spin glass. $K_xCo_zSe_2$ with $z = 1.73(4)$ is a metal, consistent with previous reports [29]. We also note that ground-state changes (Fig. 6) are concurrent with lattice parameter variations. Lattice parameters a and c for $I4/m$ show a general drop as z is increased, in contrast to lattice parameters of $I4/mmm$. When the ferromagnetism emerges, lattice parameter c in $I4/mmm$ rapidly increases and is saturated, similar to the temperature dependence of the Curie temperature.

It should be noted that both metallic conductivity and the total area of brighter stripe (block) regions increase with z. This could imply that the brighter stripe (block) area is metallic, whereas the matrix is semiconducting, both with and without Co doping [36,37]. The $z = 0.06(0)$ crystal shows semiconducting behavior through the entire temperature region we measured (1.8 K $\leqslant T \leqslant$ 300 K), even though the metallic brighter stripe (block) areas are present (Fig. 2). This is most likely because the connectivity of the three-dimensional metallic stripe (block) area is insufficient to create metallic percolation in the crystal.

The composite nature of our crystals and nano- to mesoscale mix of (super)conducting and semiconducting magnetic regions may also create states at interfaces [38,39]. This somewhat complicates the physical interpretation of bulk measurements. However, since in $K_xFe_{2-\delta}Se_2$ nanoscale phase

separation exists below $T_s = 560$ K [18], most of the conductivity changes below T_s should come from the metallic regions. This is supported by recent angle-resolved photoemission results where an orbital-selective Mott transition in $K_x Fe_{2-\delta} Se_2$ was observed above the crossover temperature [40]. Therefore, the absolute values of resistivity and magnetization reflect the contribution of both the semiconducting $K_2 Fe_4 Se_5$ and superconducting/metallic $K_x Fe_2 Se_2$ parts of the crystal. Obtained thermoelectric power and heat capacity are contributed by the metallic phase and the semiconducting phase, weighted by their conductivity. The estimated conductivity ratio between two phases is around $\sim 10^3$ at 180 K, which implies the contribution of the metallic region is 1000 times larger than that of the semiconducting region. Co substitution in the superconducting/metallic $K_x Fe_2 Se_2$ unit cell is likely to have a stronger effect on states associated with itinerant d_{xz}/d_{yz} orbitals, for example, via the localization effect in an orbital-selective Mott localization scenario [41,42]. Further Co substitution and disorder might enhance conductivity by raising the chemical potential and enlarging electron pockets, in agreement with our phase diagram [43–45].

IV. CONCLUSION

We have demonstrated how the structure, phase separation, transport, and magnetic property evolve with Co doping concentration in $K_x Fe_{2-y-z} Co_z Se_2$ single crystals. A rich ground-state phase diagram was discovered. By 3.5% Co doping superconductivity is suppressed, while phase separation is still present, which asserts the significance of the arrangement and connectivity of phases for superconductivity. A semiconducting spin glass was discovered in close proximity to the superconducting state in the phase diagram, similar to copper oxides. A ferromagnetic metal state emerged above $\sim 50\%$ Co concentration, in agreement with the structural changes. The metallicity becomes dominant as the area of stripe (block) phases increases; however, the connectivity of stripe phases may also be important for metallic conductivity.

[1] Y. Kamihara, T. Watanabe, M. Hirano, and H. Hosono, J. Am. Chem. Soc. **130**, 3296 (2008).

[2] S. Fujitsu, S. Matsuishi, and H. Hosono, Int. Mater. Rev. **57**, 311 (2012).

[3] J. Guo, S. Jin, G. Wang, S. Wang, K. Zhu, T. Zhou, M. He, and X. Chen, Phys. Rev. B **82**, 180520(R) (2010).

[4] A. S. Sefat, A. Huq, M. A. McGuire, R. Jin, B. C. Sales, D. Mandrus, L. M. D. Cranswick, P. W. Stephens, and K. H. Stone, Phys. Rev. B **78**, 104505 (2008).

[5] S. Matsuishi, Y. Inoue, T. Nomura, H. Yanagi, M. Hirano, and H. Hosono, J. Am. Chem. Soc. **130**, 14428 (2008).

[6] A. Leithe-Jasper, W. Schnelle, C. Geibel, and H. Rosner, Phys. Rev. Lett. **101**, 207004 (2008).

[7] S. R. Saha, N. P. Butch, K. Kirshenbaum, and J. Paglione, Phys. Rev. B **79**, 224519 (2009).

[8] Y. Mizuguchi, F. Tomioka, S. Tsuda, T. Yamaguchi, and Y. Takano, J. Phys. Soc. Jpn. **78**, 074712 (2009).

[9] H. Kotegawa, Y. Hara, S. Masaki, H. Tou, Y. Mizuguchi, and Y. Takano, Phys. C (Amsterdam, Neth.) **470**, S426 (2010).

[10] Y. Yu, C. J. Zhang, W. Tong, L. Zhang, D. Tan, L. Pi, Z. R. Yang, M. L. Tian, S. Tan, and Y. H. Zhang, New J. Phys. **14**, 023032 (2012).

[11] M. T. Li, Z. J. Feng, H. L. Yu, D. M. Deng, B. J. Kang, S. X. Cao, and J. C. Zhang, J. Magn. Magn. Mater. **324**, 3058 (2012).

[12] D. Tan, C. Zhang, C. Xi, L. Ling, L. Zhang, W. Tong, Y. Yu, G. Feng, H. Yu, L. Pi, Z. Yang, S. Tan, and Y. Zhang, Phys. Rev. B **84**, 014502 (2011).

[13] T. Qian, X.-P. Wang, W.-C. Jin, P. Zhang, P. Richard, G. Xu, X. Dai, Z. Fang, J.-G. Guo, X.-L. Chen, and H. Ding, Phys. Rev. Lett. **106**, 187001 (2011).

[14] Z. Wang, Y. J. Song, H. L. Shi, Z. W. Wang, Z. Chen, H. F. Tian, G. F. Chen, J. G. Guo, H. X. Yang, and J. Q. Li, Phys. Rev. B **83**, 140505(R) (2011).

[15] Y. Zhang, L. X. Yang, M. Xu, Z. R. Ye, F. Chen, C. He, H. C. Xu, J. Jiang, B. P. Xie, J. J. Ying, X. F. Wang, X. H. Chen, J. P. Hu, M. Matsunami, S. Kimura, and D. L. Feng, Nat. Mater. **10**, 273 (2011).

[16] W. Li, H. Ding, P. Deng, K. Chang, C. Song, K. He, L. Wang, X. Ma, J.-P. Hu, X. Chen, and Q.-K. Xue, Nat. Phys. **8**, 126 (2012).

[17] X. Ding, D.g Fang, Z. Wang, H. Yang, J. Liu, Q. Deng, G. Ma, C. Meng, Y. Hu, and H.-H. Wen, Nat. Commun. **4**, 1897 (2013).

[18] W. Bao, Q. Z. Huang, G. F. Chen, M. A. Green, D. M. Wang, J. B. He, and Y. M. Qiu, Chin. Phys. Lett. **28**, 086104 (2011).

[19] Z. P. Yin, K. Haule, and G. Kotliar, Nat. Mater. **10**, 932 (2011).

[20] P. Dai, J. Hu, and E. Dagotto, Nat. Phys. **8**, 709 (2012).

[21] H. Lei, M. Abeykoon, E. S. Bozin, K. Wang, J. B. Warren, and C. Petrovic, Phys. Rev. Lett. **107**, 137002 (2011).

[22] A. P. Hammersley, S. O. Svenson, M. Hanfland, and D. Hauserman, High Pressure Res. **14**, 235 (1996).

[23] A. C. Larson and R. B. Von Dreele, Los Alamos National Laboratory, Report No. LAUR 86-748, 1994 (unpublished).

[24] B. H. Toby, J. Appl. Crystallogr. **34**, 210 (2001).

[25] H. Lei, M. Abeykoon, E. S. Bozin, and C. Petrovic, Phys. Rev. B **83**, 180503(R) (2011).

[26] D. M. Wang, J. B. He, T.-L. Xia, and G. F. Chen, Phys. Rev. B **83**, 132502 (2011).

[27] H. Ryu, M. Abeykoon, K. Wang, H. Lei, N. Lazarevic, J. B. Warren, E. S. Bozin, Z. V. Popovic, and C. Petrovic, Phys. Rev. B **91**, 184503 (2015).

[28] H. Lei, E. S. Bozin, K. Wang, and C. Petrovic, Phys. Rev. B **84**, 060506(R) (2011).

[29] G. Huan and M. Greenblatt, J. Less Common Met. **156**, 247 (1989).

[30] J. A. Mydosh, *Spin Glasses: An Experimental Introduction* (Taylor and Francis, London, 1993).

[31] I. A. Campbell, Phys. Rev. B **37**, 9800 (1988).

[32] D. Chu, G. G. Kenning, and R. Orbach, Phys. Rev. Lett. **72**, 3270 (1994).

[33] N. Lazarevic, M. Abeykoon, P. W. Stephens, H. Lei, E. S. Bozin, C. Petrovic, and Z. V. Popovic, Phys. Rev. B **86**, 054503 (2012).

[34] N. Lazarević, M. Radonjić, M. Šćepanović, H. Lei, D. Tanasković, C. Petrovic, and Z. V. Popović, Phys. Rev. B **87**, 144305 (2013).

[35] N. Lazarević, H. Lei, C. Petrovic, and Z. V. Popović, Phys. Rev. B **84**, 214305 (2011).

[36] Y. Texier, J. Deisenhofer, V. Tsurkan, A. Loidl, D. S. Inosov, G. Friemel, and J. Bobroff, Phys. Rev. Lett. **108**, 237002 (2012).

[37] A. Charnukha, A. Cvitkovic, T. Prokscha, D. Pröpper, N. Ocelic, A. Suter, Z. Salman, E. Morenzoni, J. Deisenhofer, V. Tsurkan, A. Loidl, B. Keimer, and A. V. Boris, Phys. Rev. Lett. **109**, 017003 (2012).

[38] Y. J. Yan, M. Zhang, A. F. Wang, J. J. Ying, Z. Y. Li, W. Qin, X. G. Luo, J. Q. Li, J. Hu, and X. H. Chen, Sci. Rep. **2**, 212 (2012).

[39] S. Mukherjee, M. N. Gastiasoro, P. J. Hirschfeld, and B. M. Andersen, Phys. Rev. B **88**, 014519 (2013).

[40] M. Yi, D. H. Lu, R. Yu, S. C. Riggs, J.-H. Chu, B. Lv, Z. K. Liu, M. Lu, Y.-T. Cui, M. Hashimoto, S.-K. Mo, Z. Hussain, C. W. Chu, I. R. Fisher, Q. Si, and Z.-X. Shen, Phys. Rev. Lett. **110**, 067003 (2013).

[41] R. Yu and Q. Si, Phys. Rev. Lett. **110**, 146402 (2013).

[42] R. Yu, J.-X. Zhu, and Q. Si, Phys. Rev. Lett. **106**, 186401 (2011).

[43] T. Berlijn, P. J. Hirschfeld, and W. Ku, Phys. Rev. Lett. **109**, 147003 (2012).

[44] L. Craco, M. S. Laad, and S. Leoni, Phys. Rev. B **84**, 224520 (2011).

[45] F. Lu, J. Z. Zhao, and W. H. Wang, J. Phys. Condens. Matter **24**, 495501 (2012).